Front. Mech. Eng. 2019, 14(2): 201–212
https://doi.org/10.1007/s11465-019-0529-y

RESEARCH ARTICLE

Junjie ZHAN, Yangjun LUO

Robust topology optimization of hinge-free compliant mechanisms with material uncertainties based on a non-probabilistic field model

Abstract This paper presents a new robust topology optimization framework for hinge-free compliant mechanisms with spatially varying material uncertainties, which are described using a non-probabilistic bounded field model. Bounded field uncertainties are efficiently represented by a reduced set of uncertain-but-bounded coefficients on the basis of the series expansion method. Robust topology optimization of compliant mechanisms is then defined to minimize the variation in output displacement under constraints of the mean displacement and predefined material volume. The nest optimization problem is solved using a gradient-based optimization algorithm. Numerical examples are presented to illustrate the effectiveness of the proposed method for circumventing hinges in topology optimization of compliant mechanisms.

Keywords compliant mechanisms, robust topology optimization, hinges, uncertainty, bounded field

1 Introduction

Compliant mechanisms, which utilize strain energy to transform input energy components into a desired output displacement, are widely used in modern drive-train systems, electronic equipment, and aerospace systems. Similar structures are also applied in micro-electro-mechanical systems (MEMS) [1,2], such as MEMS-based microrobotics and bio-MEMS. Compliant mechanisms are used in engineering applications because of their "jointless" connection, ease of batch fabrication, and miniaturization.

Received September 13, 2018; accepted November 11, 2018

Junjie ZHAN, Yangjun LUO (✉)
State Key Laboratory of Structural Analysis for Industrial Equipment, School of Aeronautics and Astronautics, Dalian University of Technology, Dalian 116024, China
E-mail: yangjunluo@dlut.edu.cn

As a powerful tool for determining the optimal material distribution of continuum structures, topology optimization has become particularly important and has been applied to various structural and multidisciplinary design problems in the past decades [3,4]. Familiar topology optimization methods, including the solid isotropic material with penalization (SIMP) approach [5,6], evolutionary structural optimization [7,8], and level set method [9–11], have also been successfully used to determine the best configuration of compliant mechanisms through linear or nonlinear finite element analysis for achieving desirable output performance. An operational formulation of the objective function in topology optimization is critical in realizing the desired output performance and resisting external loads. Several objective functions, such as the flexibility-stiffness formulation by Saxena and Ananthasuresh [12], the energy efficiency formulation by Hetrick and Kota [13], and the artificial spring formulation by Sigmund [14], have been addressed in existing studies. However, a comparative study by Deepak et al. [15] showed that all these formulations provide almost similar topologies to rigid-body designs with localized compliance. In other words, these topology optimization models of compliant mechanisms tend to generate a not-truly compliant design with small hinge-like regions or even one-node connected hinges. This issue is due to the fact that rigid bodies connected by localized one-node hinges actually maximize the output work (or minimize the stored strain energy) in the mechanism. Hinges in compliant mechanisms introduce local high stresses, lead to the breaking of the hinge region, and make the structure difficult to be miniaturized. Many researchers [16–22] have developed numerical techniques and optimization models to prevent hinges in the topology design of compliant mechanisms.

In practical engineering conditions, inherent uncertainties are inevitable in structural systems during fabrication and operation. Uncertainties in material properties, loading conditions, and geometry play an important role in the

performance variation of practical engineering structures, especially for compliant mechanisms with hinge regions. Therefore, topology optimization models that consider uncertainties [23–25] have been investigated as a possible means to realize a hinge-free design for improving the reliability or robustness of compliant mechanisms. Maute and Frangopol [26] attempted to design MEMS by considering reliability constraints in a topology optimization model but obtained one-node hinges. Thus, the use of reliability-based topology optimization does not solve the problem. Lazarov et al. [27] proposed a robust topology optimization formulation that considers material and geometric uncertainties based on random field description. For the data case presented, although several of the results are hinge-free, hinge formation for compliant mechanism designs is not prevented when material uncertainties are considered.

Robust topology optimization has been applied to obtain structures and mechanisms with the lowest variability under loading, material, and manufacturing uncertainties. In many studies [28–30], formulations of robust design optimization were established based on the probability distribution assumption of uncertain variables or fields. Unlike random field theory [31–34] that requires precise probabilistic characteristics, the non-probabilistic bound field provides an alteration method to describe uncertainties with limited sample information [35]. This study investigates robust topology optimization for hinge-free compliant mechanisms with material uncertainties described by a bounded field model. The optimization objective is to minimize the variation in output displacement under constraints of the mean displacement and predefined material volume. The artificial spring formulation associated with the material interpolation scheme is adopted for the optimization formulation. Then, the topology optimization problem is solved by using the method of moving asymptotes (MMA) [36] with obtained sensitivity information. Numerical examples of an inverter and a gripper mechanism are presented to validate the proposed optimization model for the hinge-free design of compliant mechanisms.

2 Non-probabilistic description of bounded field uncertainties

2.1 Basic definition

Although random field theory [31] has been widely used for spatially varying uncertainties in loading distribution, material properties, and geometric dimensions, it requires precise information on the probability distribution and specified covariance function. In several real engineering structures, the non-probabilistic bounded field model provides an efficient alternation to describe uncertainties with limited sample information objectively.

We use the function $E(\boldsymbol{x})$ to define the uncertain Young's modulus at any material point $\boldsymbol{x}$. $E(\boldsymbol{x})$ is bounded by

$$E_{\mathrm{L}} \leqslant E(\boldsymbol{x}) \leqslant E_{\mathrm{U}}, \tag{1}$$

where E_{U} and E_{L} are the upper and lower bounds of the material uncertain field, respectively. The nominal value of bounded field uncertainties $E(\boldsymbol{x})$ is denoted by $\overline{E}=(E_{\mathrm{U}}+E_{\mathrm{L}})/2$, and the deviation is $\Delta E=(E_{\mathrm{U}}-E_{\mathrm{L}})/2$.

The material properties of structures are generally spatially continuous. In this study, the correlation function C is used to describe the spatial dependency of the uncertain Young's modulus. The correlation function depends only on the distance between two observation points $\boldsymbol{x}_1$ and $\boldsymbol{x}_2$, namely,

$$C(\boldsymbol{x}_1,\ \boldsymbol{x}_2)=\exp\left(-\frac{\|\boldsymbol{x}_1-\boldsymbol{x}_2\|^2}{{l_{\mathrm{c}}}^2}\right), \tag{2}$$

where l_{c} is the correlation length of the uncertain field.

2.2 Discretization of bounded field uncertainties

Continuous field uncertainties can be discretized into a finite number of uncertain variables $E(\boldsymbol{x}_1),E(\boldsymbol{x}_2),...,E(\boldsymbol{x}_N)$ on observation points $\boldsymbol{x}_1,\boldsymbol{x}_2,...,\boldsymbol{x}_N$, and the corresponding correction matrix $\boldsymbol{C}$ is denoted by

$$\boldsymbol{C}=\begin{bmatrix} C(\boldsymbol{x}_1,\boldsymbol{x}_1) & C(\boldsymbol{x}_1,\boldsymbol{x}_2) & \cdots & C(\boldsymbol{x}_1,\boldsymbol{x}_N) \\ C(\boldsymbol{x}_2,\boldsymbol{x}_1) & C(\boldsymbol{x}_2,\boldsymbol{x}_2) & \cdots & C(\boldsymbol{x}_2,\boldsymbol{x}_N) \\ \vdots & \vdots & \ddots & \vdots \\ C(\boldsymbol{x}_N,\boldsymbol{x}_1) & C(\boldsymbol{x}_N,\boldsymbol{x}_2) & \cdots & C(\boldsymbol{x}_N,\boldsymbol{x}_N) \end{bmatrix}_{N\times N}. \tag{3}$$

The series expansion method is used, and the uncertain field $E(\boldsymbol{x})$ is expressed by

$$E(\boldsymbol{x},\boldsymbol{\eta})=\overline{E}+\sum_{j=1}^{N}\eta_j\frac{1}{\sqrt{\lambda_j}}\boldsymbol{\psi}_j^{\mathrm{T}}\boldsymbol{C}_d(\boldsymbol{x}),\ -\Delta\leqslant\eta_j\leqslant\Delta, \tag{4}$$

where $\boldsymbol{\eta}=[\eta_1,\eta_2,...,\eta_N]^{\mathrm{T}}$ is the vector of uncorrelated uncertain coefficients, $\Delta=\min\limits_{i=1,2,...,N}\dfrac{\Delta E}{\sqrt{\lambda_1}|\boldsymbol{\psi}_1(\boldsymbol{x}_i)|}$ is the allowable limit, $\boldsymbol{C}_d(\boldsymbol{x})=[C(\boldsymbol{x},\boldsymbol{x}_1),C(\boldsymbol{x},\boldsymbol{x}_2),...,C(\boldsymbol{x},\boldsymbol{x}_N)]^{\mathrm{T}}$, λ_j and $\boldsymbol{\psi}_j$ are the eigenvalues and eigenvectors of matrix $\boldsymbol{C}$, respectively, and they are obtained from

$$[\boldsymbol{\psi}_1\ \ \boldsymbol{\psi}_2\ \ \cdots\ \ \boldsymbol{\psi}_N]^{\mathrm{T}}\boldsymbol{C}\ [\boldsymbol{\psi}_1\ \ \boldsymbol{\psi}_2\ \ \cdots\ \ \boldsymbol{\psi}_N]=\begin{bmatrix}\lambda_1 & & & \\ & \lambda_2 & & \\ & & \ddots & \\ & & & \lambda_N\end{bmatrix}. \tag{5}$$

The first eight modes $\boldsymbol{\psi}_j$ $(j=1,2,...,8)$ of the uncertain field in a square domain are illustrated in Fig. 1. As order index j increases, the obtained eigenvalues decrease. Large eigenvalues of the mode provide a large contribution. Therefore, Eq. (4) should be truncated by reserving only the first M eigenvalues and corresponding eigenvectors to reduce the computational cost. Truncated number M satisfies the following criterion.

$$\sum_{j=1}^{M}\lambda_j \geqslant (1-\varepsilon)\sum_{j=1}^{N}\lambda_j, \tag{6}$$

where ε is a small real number. In this study, we set $\varepsilon=1\times10^{-2}$.

In accordance with Eq. (4), Eq. (1) can be expressed as

$$-\Delta E \leqslant \sum_{j=1}^{N}\eta_j\frac{1}{\sqrt{\lambda_j}}\boldsymbol{\psi}_j^{\mathrm{T}}\boldsymbol{C}_d(\boldsymbol{x}) \leqslant \Delta E. \tag{7}$$

The truncation form of Eq. (7) is

$$-\Delta E \leqslant \sum_{j=1}^{M}\left(\eta_j\frac{1}{\sqrt{\lambda_j}}\boldsymbol{\psi}_j^{\mathrm{T}}\boldsymbol{C}_d(\boldsymbol{x}_i)\right) \leqslant \Delta E,\ i=1,2,...,N. \tag{8}$$

The matrix form of Eq. (8) is expressed as

$$-\Delta E \leqslant \boldsymbol{\eta}^{\mathrm{T}}\Lambda^{-1/2}\boldsymbol{\psi}^{\mathrm{T}}\boldsymbol{C}_d(\boldsymbol{x}_i) \leqslant \Delta E,\ i=1,2,...,N, \tag{9}$$

where $M\times M$ diagonal matrix $\boldsymbol{\Lambda}$ consists of M eigenvalues and $N\times M$ matrix consists of orthogonal eigenvectors $\boldsymbol{\psi}_j$ $(j=1,2,...,M)$.

Characteristic matrices $\boldsymbol{W}_i=\frac{1}{\sqrt{\boldsymbol{\Lambda}}}\boldsymbol{\Psi}^{\mathrm{T}}\frac{\boldsymbol{C}_d(\boldsymbol{x}_i)\boldsymbol{C}_d(\boldsymbol{x}_i)^{\mathrm{T}}}{\Delta E^2}\boldsymbol{\Psi}\frac{1}{\sqrt{\boldsymbol{\Lambda}}}$ are introduced to Eq. (9), and the uncertain coefficients $\boldsymbol{\eta}=[\eta_1\ \ \eta_2\ \ \ldots\ \ \eta_M]^{\mathrm{T}}$ are restricted in the following N multidimensional ellipsoid convex set, that is

$$\boldsymbol{\eta} \in \mathbb{E}=\{\boldsymbol{\eta}:\boldsymbol{\eta}^{\mathrm{T}}\boldsymbol{W}_i\boldsymbol{\eta}\leqslant 1,\ i=1,2,...,N\}. \tag{10}$$

3 Robust topology optimization of compliant mechanisms

When considering a compliant mechanism with bounded material field uncertainty $E(\boldsymbol{x})$, the output displacement response is characterized by a performance function $u_{\mathrm{out}}(E)$. $E(\boldsymbol{x})$ can be expanded by a reduced number of uncertain coefficients $\boldsymbol{\eta}$, as shown in Eq. (4); therefore, the performance function $u_{\mathrm{out}}(E)$ is mapped into the corresponding normalized performance function $u_{\mathrm{out}}(\boldsymbol{\eta})$. The upper bound $u_{\mathrm{out}}^{\mathrm{UPP}}$ and lower bound $u_{\mathrm{out}}^{\mathrm{LOW}}$ of the output displacement response are obtained by solving the following optimization problems.

$$\begin{aligned} u_{\mathrm{out}}^{\mathrm{UPP}} &= \max\ u_{\mathrm{out}}(\boldsymbol{\eta}) \\ \text{s.t. }& \boldsymbol{\eta}^{\mathrm{T}}\boldsymbol{W}_i\boldsymbol{\eta}\leqslant 1,\ i=1,2,...,N \\ & -\Delta\leqslant\eta_j\leqslant\Delta,\ j=1,2,...,M \end{aligned} \tag{11}$$

$$\begin{aligned} u_{\mathrm{out}}^{\mathrm{LOW}} &= \min\ u_{\mathrm{out}}(\boldsymbol{\eta}) \\ \text{s.t. }& \boldsymbol{\eta}^{\mathrm{T}}\boldsymbol{W}_i\boldsymbol{\eta}\leqslant 1,\ i=1,2,...,N \\ & -\Delta\leqslant\eta_j\leqslant\Delta,\ j=1,2,...,M \end{aligned} \tag{12}$$

The nominal and deviation values of the performance function $u_{\mathrm{out}}(E)$ are calculated as follows:

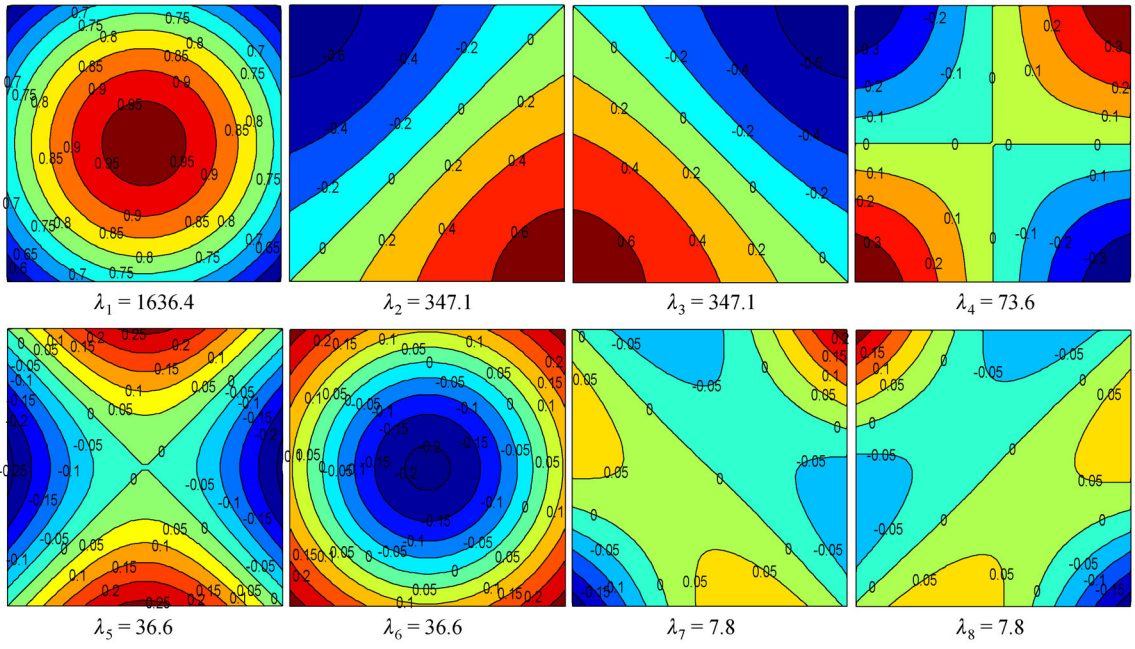

Fig. 1 First eight modes $\boldsymbol{\psi}_j$ $(j=1,2,...,8)$ in the series expansion of field uncertainties

$$\overline{u}_{\text{out}}=(u_{\text{out}}^{\text{UPP}}+u_{\text{out}}^{\text{LOW}})/2, \tag{13}$$

$$\Delta u_{\text{out}}=(u_{\text{out}}^{\text{UPP}}-u_{\text{out}}^{\text{LOW}})/2. \tag{14}$$

On the basis of the framework of non-probabilistic uncertain field, the robust topology optimization problem of compliant mechanisms is formulated using the nominal value and the deviation of output displacement as follows:

$$\begin{aligned}&\min_{\boldsymbol{\rho}}\ \Delta u_{\text{out}},\\&\text{s.t.}\ \ \boldsymbol{K}(\tilde{\boldsymbol{\rho}},\boldsymbol{\eta})\cdot\boldsymbol{u}(\tilde{\boldsymbol{\rho}},\boldsymbol{\eta})=\boldsymbol{F},\\&\qquad \overline{u}_{\text{out}}+u^{*}\leqslant 0,\\&\qquad \sum_{e=1}^{N_{\text{e}}}\tilde{\rho}_e V_e\leqslant V^{*},\\&\qquad 0\leqslant\rho_e\leqslant 1,\ e=1,2,...,N_{\text{e}},\end{aligned} \tag{15}$$

where the design variables $\boldsymbol{\rho}=[\rho_1,\rho_2,...,\rho_{N_{\text{e}}}]^{\text{T}}$ are the vector of elemental relative densities, $\tilde{\rho}_e$ is the result of Heaviside projection filtering for the design variable ρ_e, N_{e} is the number of finite elements of the entire design domain, $\boldsymbol{K}$ denotes the global stiffness matrix of the physical problem obtained by the finite element discretization, $\boldsymbol{u}$ and $\boldsymbol{F}$ are the displacement and force vectors, respectively, u^{*} is a given displacement constraint on the nominal value of the output displacement response, V_e is the volume of element e, and V^{*} is the allowed total volume of the solid material.

The material Young's modulus of the eth element, E_e, is obtained by using the SIMP model [37] as follows:

$$E_e=E_{\min}+\tilde{\rho}_e^{p}(E(\boldsymbol{x}_e)-E_{\min}), \tag{16}$$

where $E(\boldsymbol{x}_e)$ denotes the Young's modulus of the fully solid material in the eth element, which is an uncertain variable, as described in Eq. (4). $p=3$ is the penalty factor, and $E_{\min}$ is given a small positive value to avoid stiffness singularity in the finite element analysis.

The objective and constraint functions in the optimization problem Eq. (15) are solved by the sub-problems in Eqs. (11) and (12). Thus, robust topology optimization of compliant mechanisms is considered a nested optimization problem. In this study, we focus on the topology optimization of compliant mechanisms in a linear elastic setting.

The smoothed projection function [38] (approximate Heaviside function) for filtering relative densities is adopted in this study to suppress mesh dependency and checkerboard patterns and acquire a clear topology.

$$\tilde{\rho}_e=\frac{\tanh(\beta\eta)+\tanh(\beta(\overline{\rho}_e-\eta))}{\tanh(\beta\eta)+\tanh(\beta(1-\eta))}, \tag{17}$$

where $\overline{\rho}_e=\dfrac{\sum_{i=1}^{Q}w(\boldsymbol{x}_i)v_i\rho_i}{\sum_{i=1}^{Q}w(\boldsymbol{x}_i)v_i}$ is the average density value of the element e in the neighborhood region Q, $w(\boldsymbol{x}_i)$ is the weight, v_i is the elemental volume, β denotes the smoothing parameter, and η is the threshold. If parameter β approaches zero, then the value of approximate Heaviside function $\tilde{\rho}_e$ is approximately equal to average density $\overline{\rho}_e$. In this study, the value of threshold η is 0.5. The Heaviside functions for $\eta=0.5$ with different values of β are illustrated in Fig. 2. In a practical optimization process, the initial value of parameter β is 1, and it increases to 128 by multiplying 2 every 40 iterations.

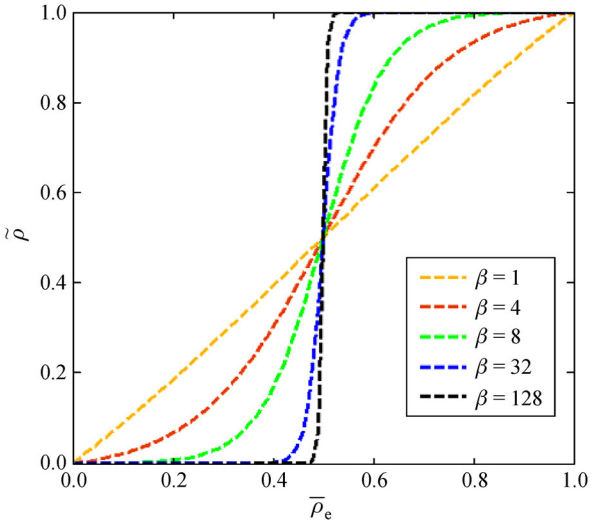

Fig. 2 Approximate Heaviside function with different values of β

4 Sensitivity analysis and algorithm flowchart

4.1 Sensitivity analysis of inner-loop optimization problems

The adjoint method is used to calculate the sensitivity of the objective function in the inner-loop optimization problems in Eqs. (11) and (12). The chain rule of differentiation is used, and the sensitivity of the performance function $u_{\text{out}}(\boldsymbol{\eta})$ with respect to uncertain coefficients η_j is

$$\frac{\partial u_{\text{out}}}{\partial\eta_j}=\left(\frac{\partial u_{\text{out}}}{\partial\boldsymbol{u}}\right)^{\text{T}}\frac{\mathrm{d}\boldsymbol{u}}{\mathrm{d}\boldsymbol{E}}\frac{\mathrm{d}\boldsymbol{E}}{\mathrm{d}\eta_j},\ j=1,2,...,M, \tag{18}$$

where $\boldsymbol{u}$ is the nodal displacement vector of the compliant mechanism and $\boldsymbol{E}=[E_1,E_2,...,E_{N_{\text{e}}}]^{\text{T}}$ is the vector of the elemental elastic modulus.

By taking the derivative of the equilibrium equation $\boldsymbol{K}\boldsymbol{u}=\boldsymbol{F}$, we have

$$\boldsymbol{K}\frac{\mathrm{d}\boldsymbol{u}}{\mathrm{d}E_i}=\frac{\mathrm{d}\boldsymbol{F}}{\mathrm{d}E_i}-\frac{\mathrm{d}\boldsymbol{K}}{\mathrm{d}E_i}\boldsymbol{u},\ i=1,2,...,N_{\text{e}}. \tag{19}$$

In this study, external load $\boldsymbol{F}$ does not depend on the

material elastic modulus; therefore, the first term on the right side of Eq. (19) must vanish.

Substituting Eq. (19) into Eq. (18), we obtain

$$\frac{\partial u_{\text{out}}}{\partial \eta_j}=\left(\frac{\partial u_{\text{out}}}{\partial \boldsymbol{u}}\right)^{\mathrm{T}}\boldsymbol{K}^{-1}\sum_{i=1}^{N}\left(-\frac{\mathrm{d}\boldsymbol{K}}{\mathrm{d}E_i}\boldsymbol{u}\right)\frac{\mathrm{d}E_i}{\mathrm{d}\eta_j}. \tag{20}$$

The adjoint vector $\boldsymbol{\lambda}$ is introduced to satisfy the equation

$$\boldsymbol{K}\boldsymbol{\lambda}=\frac{\partial u_{\text{out}}}{\partial \boldsymbol{u}}. \tag{21}$$

Equation (20) becomes

$$\frac{\partial u_{\text{out}}}{\partial \eta_j}=\sum_{i=1}^{N}\left(-\boldsymbol{\lambda}^{\mathrm{T}}\frac{\mathrm{d}\boldsymbol{K}}{\mathrm{d}E_i}\boldsymbol{u}\cdot\frac{\mathrm{d}E_i}{\mathrm{d}\eta_j}\right),\ j=1,2,...,M. \tag{22}$$

The observation point is assumed to coincide with the finite element center point, and the sensitivity of structural stiffness matrix $\boldsymbol{K}$ with respect to E_i can be obtained by calculation from each element. Equation (22) can be rewritten as

$$\frac{\partial u_{\text{out}}}{\partial \eta_j}=\sum_{i=1}^{N}\left(-\boldsymbol{\lambda}_i{}^{\mathrm{T}}\frac{\mathrm{d}\boldsymbol{K}_i}{\mathrm{d}E_i}\boldsymbol{u}_i\cdot\frac{\mathrm{d}E_i}{\mathrm{d}\eta_j}\right),\ j=1,2,...,M. \tag{23}$$

where $\boldsymbol{\lambda}_i$ is the adjoint vector of the ith element and $\boldsymbol{K}_i$ and $\boldsymbol{u}_i$ are the element stiffness matrix and element displacement vector, respectively.

4.2 Sensitivity analysis of the outer-loop optimization problem

In the outer-loop optimization problem, the objective and constraint functions include the calculation of the upper bound $u_{\text{out}}^{\text{UPP}}$ and lower bound $u_{\text{out}}^{\text{LOW}}$ of the output displacement. The sensitivity of the two bounds (generally denoted by $u_{\text{out}}(\boldsymbol{\rho},\boldsymbol{\eta}^*)$, where $\boldsymbol{\eta}^*$ is the solution of the inner-loop problem Eq. (11) or (12)) with respect to the design variables is determined as follows.

The sensitivity of $u_{\text{out}}(\boldsymbol{\rho},\boldsymbol{\eta}^*)$ with respect to $\tilde{\rho}_e$ is expressed as

$$\frac{\mathrm{d}u_{\text{out}}(\boldsymbol{\rho},\boldsymbol{\eta}^*)}{\mathrm{d}\tilde{\rho}_e}=\frac{\partial u_{\text{out}}(\boldsymbol{\rho},\boldsymbol{\eta}^*)}{\partial \tilde{\rho}_e}+\sum_{j=1}^{M}\left(\frac{\partial u_{\text{out}}(\boldsymbol{\rho},\boldsymbol{\eta}^*)}{\partial \eta_j}\cdot\frac{\partial \eta_j}{\partial \tilde{\rho}_e}\right). \tag{24}$$

The minimum or maximum performance function should satisfy Karush-Kuhn-Tucker conditions, that is

$$\frac{\partial u_{\text{out}}(\boldsymbol{\rho},\boldsymbol{\eta}^*)}{\partial \eta_j}+\sum_{i=1}^{N}2\gamma_i\boldsymbol{\eta}^{\mathrm{T}}\boldsymbol{W}_i\frac{\partial \boldsymbol{\eta}}{\partial \eta_j}=\boldsymbol{0}, \tag{25}$$

$$\gamma_i\geqslant 0, \tag{26}$$

$$\boldsymbol{\eta}^{\mathrm{T}}\boldsymbol{W}_i\boldsymbol{\eta}-1=0,\ i=1,2,...,N, \tag{27}$$

where γ_i is the Lagrangian multiplier that corresponds to the ith constraint.

Using Eqs. (24) and (25), we obtain

$$\frac{\mathrm{d}u_{\text{out}}(\boldsymbol{\rho},\boldsymbol{\eta}^*)}{\mathrm{d}\tilde{\rho}_e}=\frac{\partial u_{\text{out}}(\boldsymbol{\rho},\boldsymbol{\eta}^*)}{\partial \tilde{\rho}_e}+\sum_{j=1}^{M}\left(-\sum_{i=1}^{N}2\gamma_i\boldsymbol{\eta}^{\mathrm{T}}\boldsymbol{W}_i\frac{\partial \boldsymbol{\eta}}{\partial \eta_j}\cdot\frac{\partial \eta_j}{\partial \tilde{\rho}_e}\right). \tag{28}$$

Taking the derivative of Eq. (27) with respect to $\tilde{\rho}_e$ yields

$$\frac{\mathrm{d}(\boldsymbol{\eta}^{\mathrm{T}}\boldsymbol{W}_i\boldsymbol{\eta}-1)}{\mathrm{d}\tilde{\rho}_e}=\sum_{j=1}^{M}2\boldsymbol{\eta}^{\mathrm{T}}\boldsymbol{W}_i\frac{\partial \boldsymbol{\eta}}{\partial \eta_j}\cdot\frac{\mathrm{d}\eta_j}{\mathrm{d}\tilde{\rho}_e}=\boldsymbol{0}. \tag{29}$$

Submitting Eq. (29) into Eq. (28), we have

$$\frac{\mathrm{d}u_{\text{out}}(\boldsymbol{\rho},\boldsymbol{\eta}^*)}{\mathrm{d}\tilde{\rho}_e}=\frac{\partial u_{\text{out}}(\boldsymbol{\rho},\boldsymbol{\eta}^*)}{\partial \tilde{\rho}_e}. \tag{30}$$

The sensitivity of the performance function can be easily evaluated by using the adjoint method, namely,

$$\frac{\partial u_{\text{out}}(\boldsymbol{\rho},\boldsymbol{\eta}^*)}{\partial \tilde{\rho}_e}=-\boldsymbol{\psi}^{\mathrm{T}}\frac{\mathrm{d}\boldsymbol{K}(\boldsymbol{\eta}^*)}{\mathrm{d}\tilde{\rho}_e}\boldsymbol{u}(\boldsymbol{\eta}^*), \tag{31}$$

where

$$\boldsymbol{\psi}=\boldsymbol{K}^{-1}(\boldsymbol{\eta}^*)\frac{\partial u_{\text{out}}}{\partial \boldsymbol{u}}. \tag{32}$$

The sensitivities of the output displacement bounds with respect to design variable ρ_e are calculated by using the chain rule

$$\frac{\mathrm{d}u_{\text{out}}(\boldsymbol{\rho},\boldsymbol{\eta}^*)}{\mathrm{d}\rho_e}=\sum_{i=1}^{Q}\frac{\partial u_{\text{out}}(\boldsymbol{\rho},\boldsymbol{\eta}^*)}{\partial \tilde{\rho}_i}\frac{\partial \tilde{\rho}_i}{\partial \overline{\rho}_i}\frac{\partial \overline{\rho}_i}{\partial \rho_e}, \tag{33}$$

where

$$\frac{\partial \overline{\rho}_e}{\partial \rho_i}=\frac{w(\boldsymbol{x}_i)v_i}{\sum_{i=1}^{Q}w(\boldsymbol{x}_j)v_j}, \tag{34}$$

and

$$\frac{\partial \tilde{\rho}_i}{\partial \overline{\rho}_i}=\frac{\beta(\operatorname{sech}(\beta(\overline{\rho}_i-\eta)))^2}{\tanh(\beta\eta)+\tanh(\beta(1-\eta))}. \tag{35}$$

4.3 Flowchart of the optimization algorithm

The flowchart for solving the nested optimization problem is shown in Fig. 3. In this figure, the left part is the outer-loop process, which is used to update the material relative

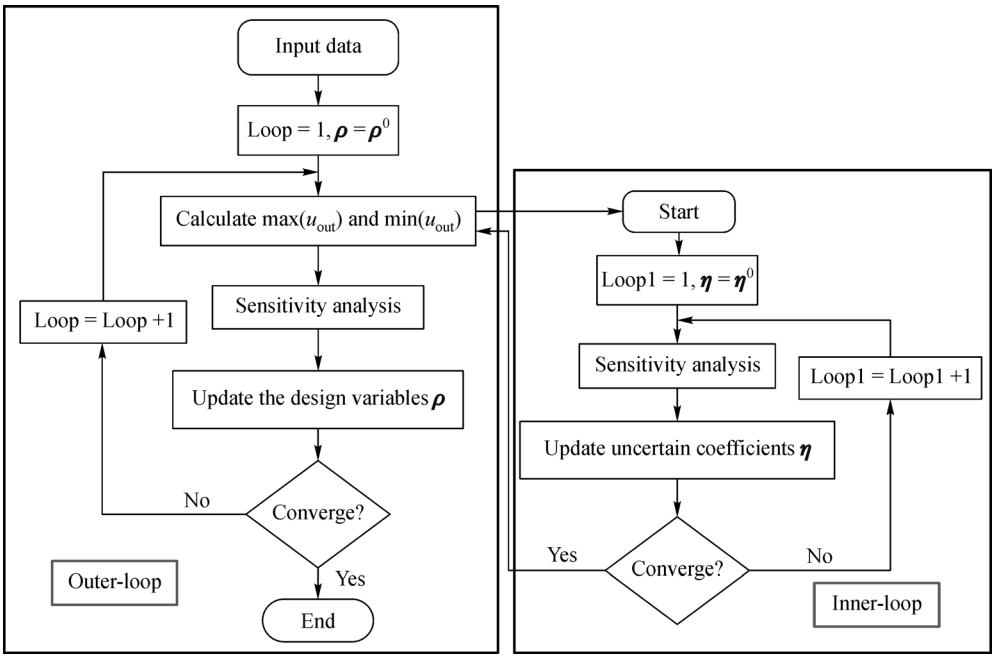

Fig. 3 Flowchart for solving the nested optimization problem

densities; the right part is the inner-loop iteration, which is used to find the maximum and minimum values of output displacement. In this study, the outer- and inner-loop optimization problems are solved by using the MMA.

5 Numerical examples

We present two examples for robust topology optimization of compliant mechanisms with an uncertain field in material elastic modulus. The uncertain Young's modulus is bounded in the interval [0.5,0.9], and the Poisson's ratio is 0.3. In both examples, the structure is assumed to be symmetrical, which means the upper and lower halves of the design domain share the same design variables. However, the uncertain material field applied to the entire structure is asymmetrical.

5.1 Robust topology optimization of a compliant inverter

The design of a compliant inverter is considered in this example, and the aim is to determine the optimal structure that converts an input load on one side into a displacement in the opposite direction on the other side. As shown in Fig. 4, the dimension of the design domain is 120×120. A horizontal load $F_{in}=1$ is applied to the input point, and the spring stiffness is set to $k_{in}=k_{out}=0.02$. The allowable material volume fraction is 30%.

In this example, two different values of correlation length, $l_c=120$ and $l_c=60$, are tested. We consider that the truncation error is less than 1%. The first 6 eigenvectors are selected in the series expansion of the bounded field

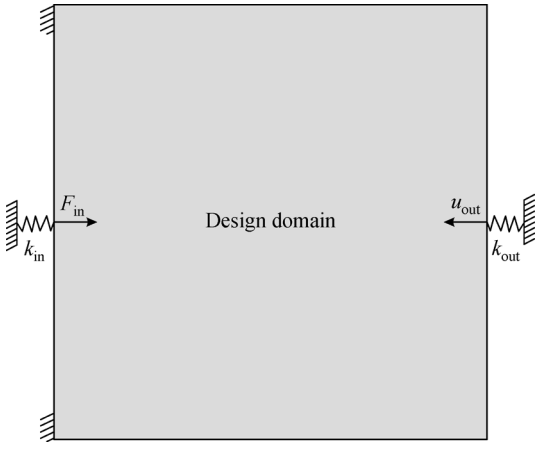

Fig. 4 Design domain and boundary conditions of a compliant inverter

uncertainty when $l_c=120$, and the first 12 eigenvectors are selected when $l_c=60$.

Figure 5 shows the optimal robust solutions of the compliant inverter with the correlation length $l_c=120$ by using the proposed method. In Fig. 5, the left column gives the optimal topologies of the inverter considering different displacement constraints ($u^*=16$, 15, 14, 13, and 12), and the middle and right columns show the worst- and best-case realization of the uncertain field, respectively. As shown in Fig. 5, with decreases in the allowable nominal value of output displacement u^*, the objective value Δu_{out} of the obtained compliant inverter design decreases. The output displacement becomes increasingly robust with respect to variations in the Young's modulus bound

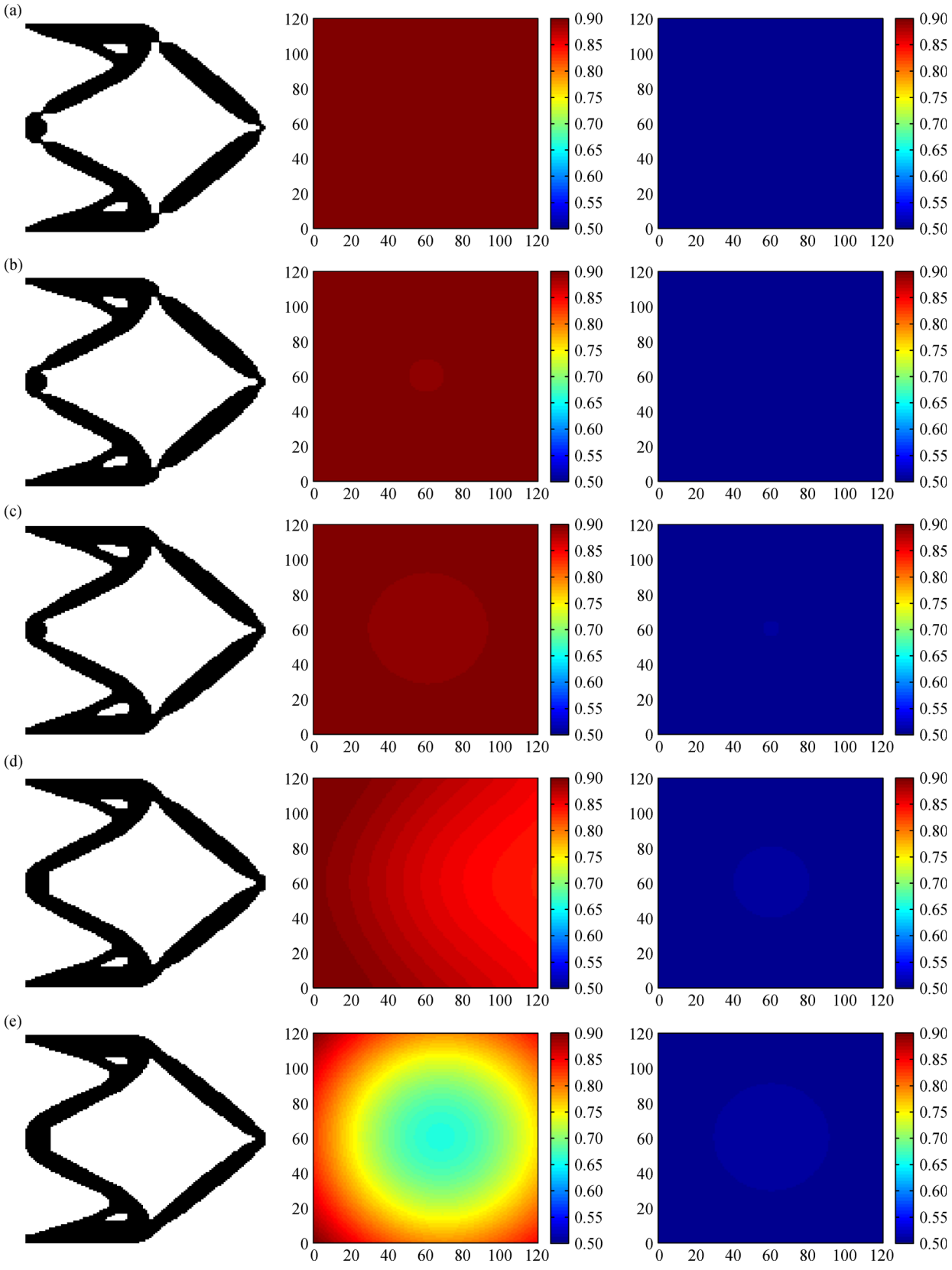

Fig. 5 Optimized topologies (left), worst-case realization (middle), and best-case realization (right) of uncertain field for the compliant inverter when $l_c=120$. (a) $u^*=16$, $\Delta u_{out}=1.562$; (b) $u^*=15$, $\Delta u_{out}=1.293$; (c) $u^*=14$, $\Delta u_{out}=0.965$; (d) $u^*=13$, $\Delta u_{out}=0.731$; (e) $u^*=12$, $\Delta u_{out}=0.550$

[0.5,0.9]. The results also demonstrate that hinges in the optimal design gradually vanish when the deviation value of the performance function increases. Therefore, the proposed robust topology optimization model is an effective means of avoiding the appearance of hinges in the design of compliant mechanisms.

The iteration histories of the optimization process for the compliant inverter are plotted in Fig. 6. The histories show a convergence of the objective function for each case. The evolution histories present minimal turbulence because of the changed parameter β in the Heaviside function.

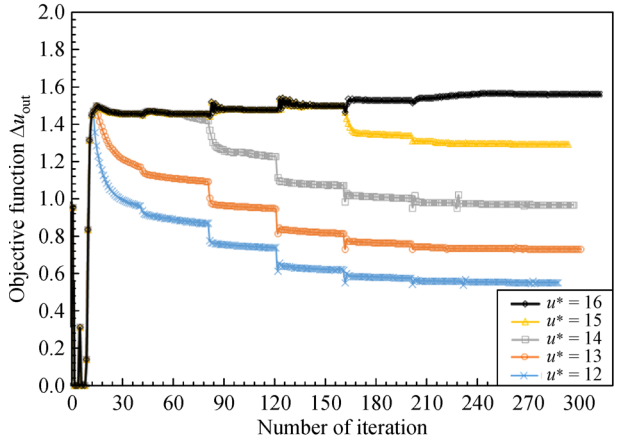

Fig. 6 Iteration histories for the compliant inverter when $l_c = 120$

Figure 7 shows the nominal value and corresponding deviation range of the output displacement for topological configurations in Figs. 5(a)–5(e) when $l_c = 120$. The nominal value of the output displacement response of the topological configuration in Fig. 5(a) is greater than that of the designs in Figs. 5(b)–5(e). The topological configuration in Fig. 5(e) is the most robust because it gains the smallest deviation value of output displacement. As expected, the topological configuration in Fig. 5(a) has obvious one-node hinges, whereas no hinges are found in the topological configuration in Fig. 5(e).

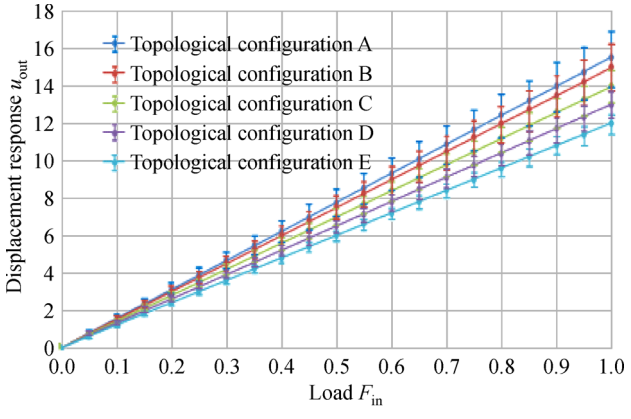

Fig. 7 Nominal value and deviation range of output displacement versus F_{in} for topological configurations in Figs. 5(a)–5(e) when $l_c = 120$

The robust design solutions of the compliant inverter when the correlation length is $l_c = 60$ are shown in Fig. 8. The left column indicates that no hinges exist in the optimal topologies of the inverter in Figs. 8(c)–5(e). This finding validates that the present robust optimization can minimize the variation in the output displacement of compliant mechanisms and thus avoid hinges that may lead to serious losses arising from uncertainties. Compared with the solutions in Fig. 5 with a relatively large correlation length, the worst- and best-case realizations in Fig. 8 have relatively intense changes in the distribution of material field uncertainty when $l_c = 60$.

Comparison of the optimized topologies (left) in Figs. 5 and 8 shows that the topological configurations differ and have different correlation lengths when the same value of u^* is defined. The middle parts of Figs. 5 and 8 depict that the worst-case realizations of the uncertain material field for the compliant inverter are distinctly different. As a result, the objective functions of the former with a large correlation length are greater than those of the latter with a small correlation length. Therefore, the correlation length of the uncertain field plays an important role in the optimal topology design of compliant mechanisms.

5.2 Robust topology optimization of a compliant gripper

The design domain and boundary conditions of a compliant gripper are shown in Fig. 9. The size of the design domain is 120×120, and the design domain is correspondingly divided into 120×120 finite elements. The size of the square hole in the gripper is 30×30. The spring stiffness is set to $k_{in} = 0.02$, $k_{out1} = k_{out2} = 0.012$, and the input force for the compliant gripper is $F_{in} = 1$. For this compliant gripper, the performance function u_{out} is the relative difference between displacements u_{out1} and u_{out2} of two output points, which is denoted as $u_{out} = |u_{out1}| + |u_{out2}|$. The allowable material volume fraction is 30%. Two different correlation lengths, $l_c = 60$ and $l_c = 30$, are considered for the bounded field uncertainty in material elastic modulus.

In the case of $l_c = 60$, robust topology optimization with different values of the nominal performance function constraint, i.e., $u^* = 26$, 24, and 22, is performed by using the proposed method, and the results are shown in Fig. 10. The corresponding optimal topologies, worst-case realization, and best-case realization are plotted in the left, middle, and right columns, respectively. The optimal topologies in Fig. 10 imply that with the decrease in the nominal value of the performance function, the compliant gripper design gains improved robustness with respect to uncertainties, and the hinges are prevented gradually. This

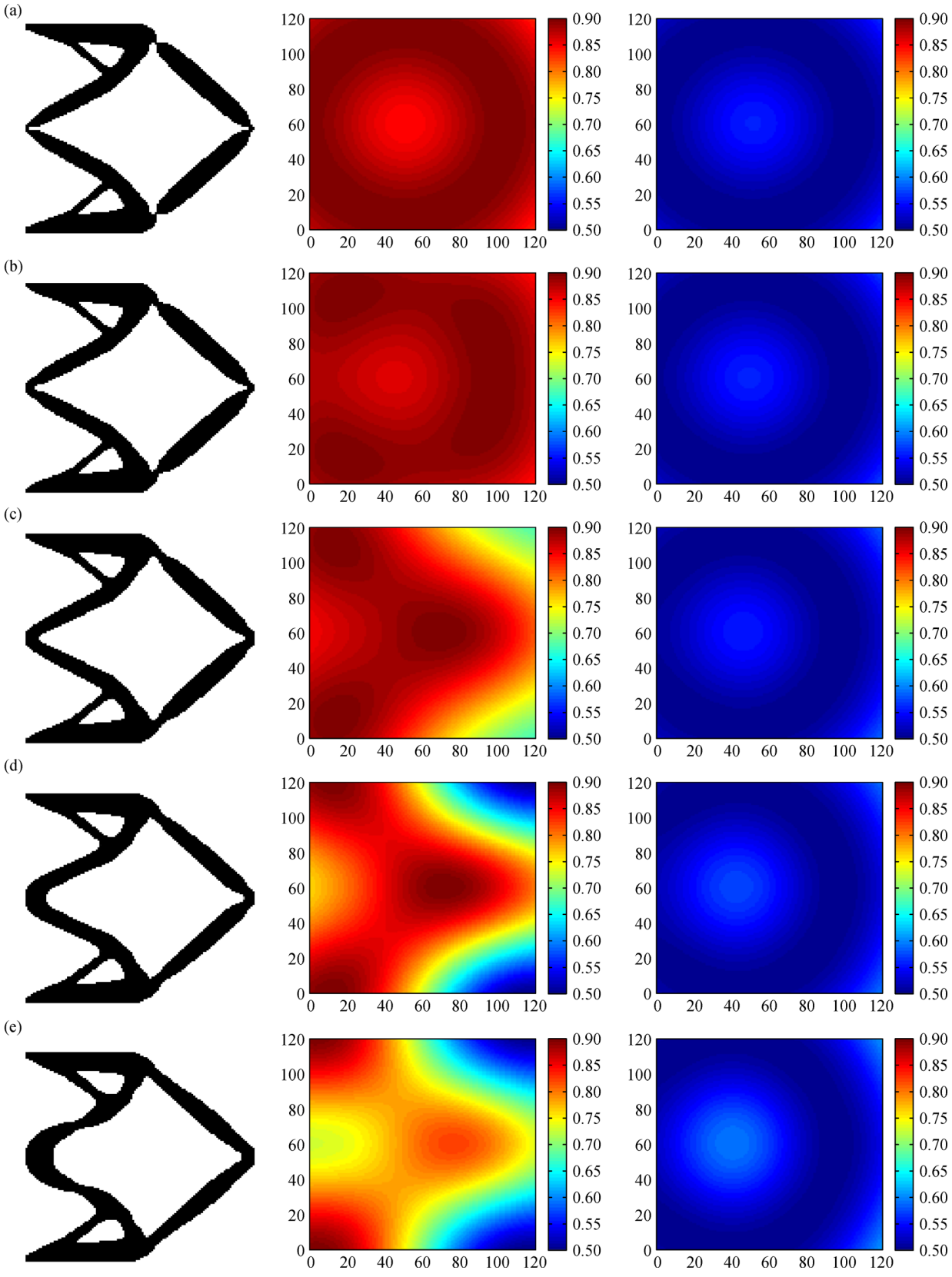

Fig. 8 Optimized topologies (left), worst-case realization (middle), and best-case realization (right) of uncertain field for the compliant inverter when $l_c=60$. (a) $u^*=16$, $\Delta u_{out}=1.495$; (b) $u^*=15$, $\Delta u_{out}=1.165$; (c) $u^*=14$, $\Delta u_{out}=0.900$; (d) $u^*=13$, $\Delta u_{out}=0.698$; (e) $u^*=12$, $\Delta u_{out}=0.535$

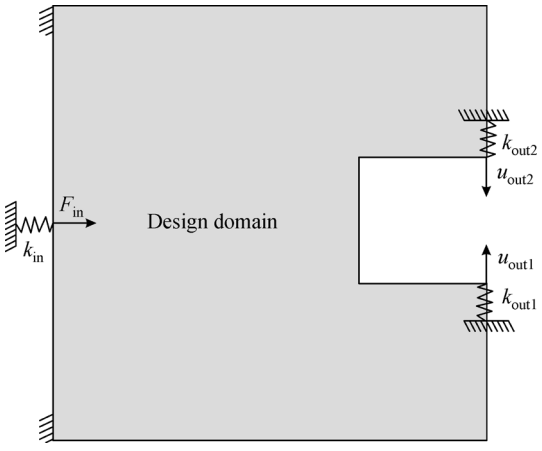

Fig. 9 Design domain and boundary conditions of a compliant gripper

result verifies that the proposed method is effective for circumventing hinges in the topology design of compliant mechanisms.

The robust design solutions for the compliant gripper mechanism with different nominal output performances when the correlation length of the uncertain material field is decreased to $l_c = 30$ are shown in Fig. 11. The worst-case realizations have a relatively intense change in the distribution surface of the material field uncertainty compared with that of the case of $l_c = 60$ in Fig. 9. When the nominal performance function constraint is $u^* = 26$, the deviation in output displacement for the final solution is large, i.e., $\Delta u_{out} = 2.882$, and one-node hinges can be observed clearly in the optimal topology. When $u^* = 22$, the deviation in output displacement for the final hinge-free design decreases to $\Delta u_{out} = 1.617$, which means the compliant mechanism is more capable of resisting uncertainties than that with $u^* = 26$.

6 Conclusions

A robust topology optimization method for compliant mechanisms with bounded field uncertainties in material

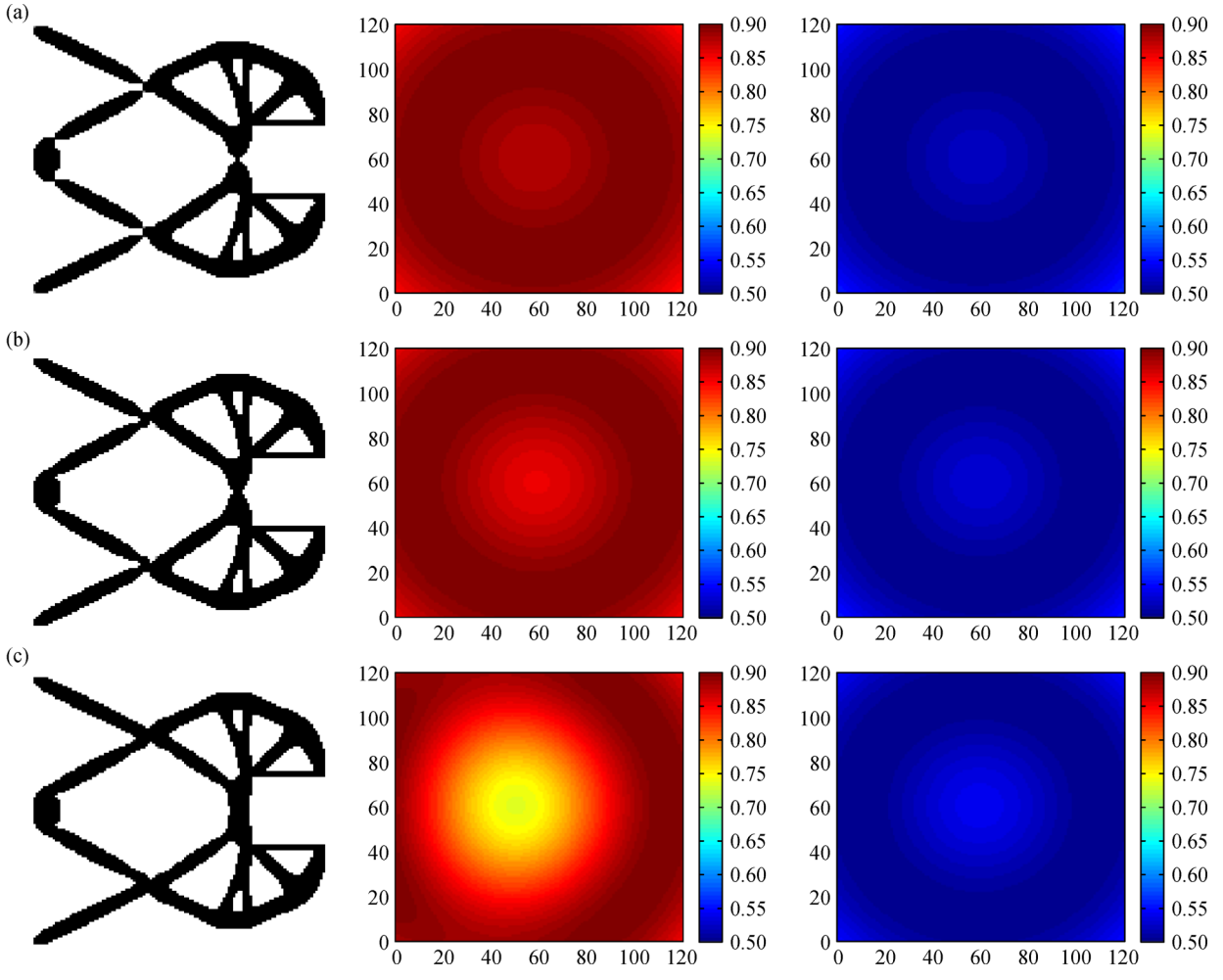

Fig. 10 Optimized topologies (left), worst-case realization (middle), and best-case realization (right) of uncertain field for the compliant gripper when $l_c = 60$. (a) $u^* = 26$, $\Delta u_{out} = 2.804$; (b) $u^* = 24$, $\Delta u_{out} = 1.999$, (c) $u^* = 22$, $\Delta u_{out} = 1.468$

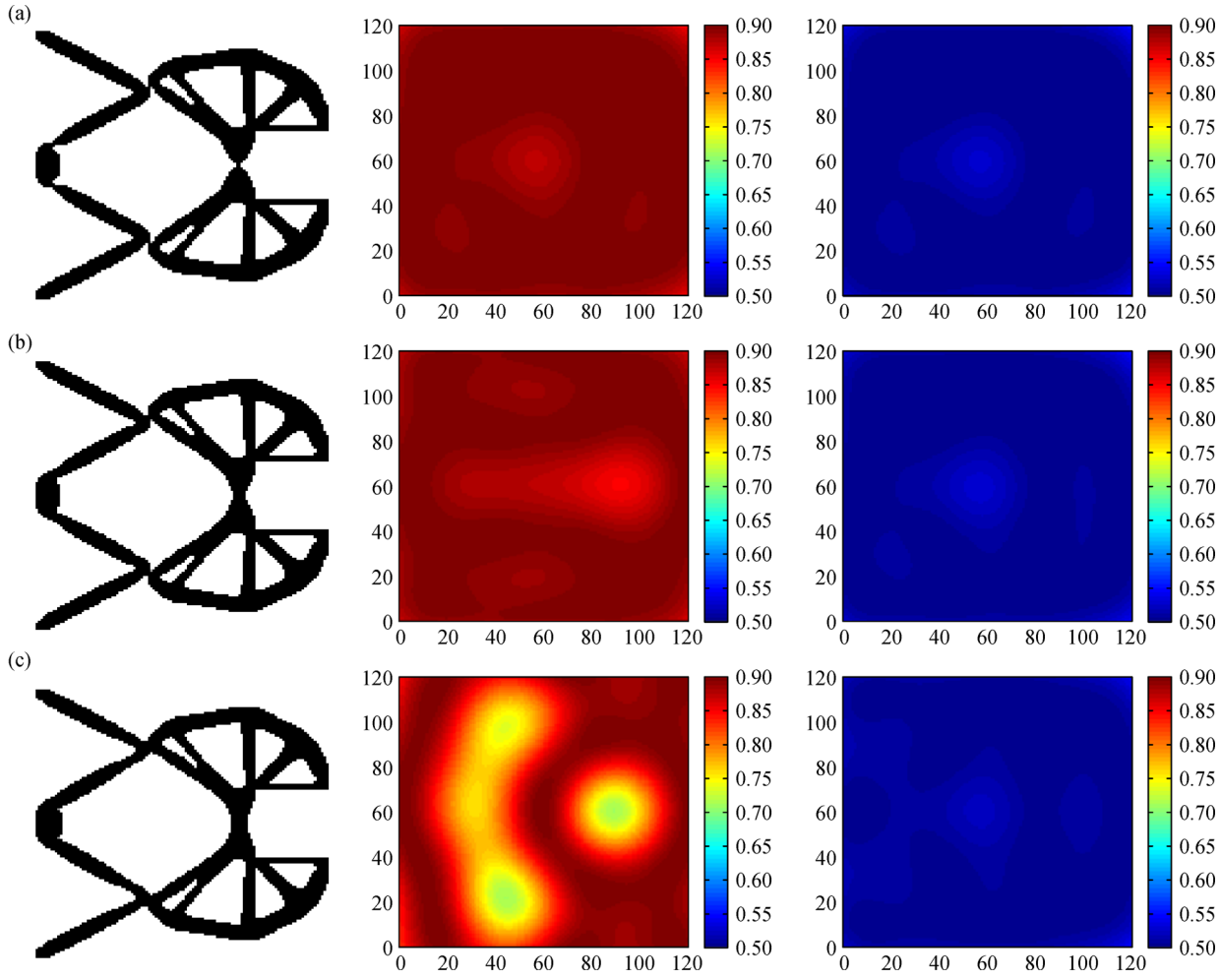

Fig. 11 Optimized topologies (left), worst-case realization (middle), and best-case realization (right) of uncertain field for the compliant gripper when $l_c=30$. (a) $u^*=26$, $\Delta u_{out}=2.882$; (b) $u^*=24$, $\Delta u_{out}=2.131$; (c) $u^*=22$, $\Delta u_{out}=1.617$

properties is proposed in this study. The method of series expansion is employed for the dimension reduction of non-probabilistic bounded field uncertainties. Robust topology optimization of compliant mechanisms is considered a nested optimization problem. In the optimization process, we take the nominal value of the output displacement response as a constraint and minimize the robustness of the compliant mechanism. The effect of the correlation length of bounded field uncertainties on the optimal topologies is also investigated.

The applicability of the proposed robust topology optimization for compliant mechanisms with material bounded field uncertainties is illustrated by two numerical examples. The results show that the robustness of the optimal design of compliant mechanisms increases with the decrease in the nominal value of the performance function. Moreover, robust topology optimization of compliant mechanisms considering material uncertainties can successfully prevent the formation of hinges.

Acknowledgements This work was financially supported by the National Key R&D Program of China (Grant No. 2017YFB0203604) and the National Natural Science Foundation of China (Grant No. 11472215).

References

1. Shi F, Ramesh P, Mukherjee S. Simulation methods for micro-electro-mechanical structures (MEMS) with application to a microtweezer. Computers & Structures, 1995, 56(5): 769–783
2. Kota S, Joo J, Li Z, et al. Design of compliant mechanisms: Applications to MEMS. Analog Integrated Circuits and Signal Processing, 2001, 29(1–2): 7–15
3. Sigmund O, Maute K. Topology optimization approaches. Structural and Multidisciplinary Optimization, 2013, 48(6): 1031–1055
4. Deaton J D, Grandhi R V. A survey of structural and multidisciplinary continuum topology optimization: Post 2000. Structural and Multidisciplinary Optimization, 2014, 49(1): 1–38
5. Pedersen C B W, Buhl T, Sigmund O. Topology synthesis of large-displacement compliant mechanisms. International Journal for Numerical Methods in Engineering, 2001, 50(12): 2683–2705
6. Lee E, Gea H C. A strain based topology optimization method for

compliant mechanism design. Structural and Multidisciplinary Optimization, 2014, 49(2): 199–207
7. Ansola R, Veguería E, Canales J, et al. A simple evolutionary topology optimization procedure for compliant mechanism design. Finite Elements in Analysis and Design, 2007, 44(1–2): 53–62
8. Huang X, Li Y, Zhou S W, et al. Topology optimization of compliant mechanisms with desired structural stiffness. Engineering Structures, 2014, 79: 13–21
9. Luo Z, Tong L. A level set method for shape and topology optimization of large-displacement compliant mechanisms. International Journal for Numerical Methods in Engineering, 2008, 76(6): 862–892
10. Zhu B, Zhang X. A new level set method for topology optimization of distributed compliant mechanism. International Journal for Numerical Methods in Engineering, 2012, 91(8): 843–871
11. Luo Z, Zhang N, Ji J, et al. A meshfree level-set method for topological shape optimization of compliant multiphysics actuators. Computer Methods in Applied Mechanics and Engineering, 2012, 223–224: 133–152
12. Saxena A, Ananthasuresh G K. On an optimal property of compliant topologies. Structural and Multidisciplinary Optimization, 2000, 19(1): 36–49
13. Hetrick J A, Kota S. An energy formulation for parametric size and shape optimization of compliant mechanisms. Journal of Mechanical Design, 1999, 121(2): 229–234
14. Sigmund O. On the design of compliant mechanisms using topology optimization. Mechanics Based Design of Structures and Machines, 1997, 25(4): 493–524
15. Deepak S R, Dinesh M, Sahu D K, et al. A comparative study of the formulations and benchmark problems for the topology optimization of compliant mechanisms. Journal of Mechanisms and Robotics, 2009, 1(1): 011003
16. Poulsen T A. A simple scheme to prevent checkerboard patterns and one-node connected hinges in topology optimization. Structural and Multidisciplinary Optimization, 2002, 24(5): 396–399
17. Wang N, Zhang X. Compliant mechanisms design based on pairs of curves. Science China. Technological Sciences, 2012, 55(8): 2099–2106
18. Luo Z, Chen L, Yang J, et al. Compliant mechanisms design using multi-objective topology optimization scheme of continuum structures. Structural and Multidisciplinary Optimization, 2005, 30(2): 142–154
19. Zhu B, Zhang X, Wang N. Topology optimization of hinge-free compliant mechanisms with multiple outputs using level set method. Structural and Multidisciplinary Optimization, 2013, 47(5): 659–672
20. Zhu B, Zhang X, Fatikow S. A multi-objective method of hinge-free compliant mechanism optimization. Structural and Multidisciplinary Optimization, 2014, 49(3): 431–440
21. Lopes C G, Novotny A A. Topology design of compliant mechanisms with stress constraints based on the topological derivative concept. Structural and Multidisciplinary Optimization, 2016, 54(4): 737–746
22. de Assis Pereira A, Cardoso E L. On the influence of local and global stress constraint and filtering radius on the design of hinge-free compliant mechanisms. Structural and Multidisciplinary Optimization, 2018, 58(2): 641–655
23. Luo Y, Kang Z, Luo Z, et al. Continuum topology optimization with non-probabilistic reliability constraints based on multi-ellipsoid convex model. Structural and Multidisciplinary Optimization, 2009, 39(3): 297–310
24. Chen S, Chen W, Lee S. Level set based robust shape and topology optimization under random field uncertainties. Structural and Multidisciplinary Optimization, 2010, 41(4): 507–524
25. Luo Y, Zhou M, Wang M Y, et al. Reliability based topology optimization for continuum structures with local failure constraints. Computers & Structures, 2014, 143: 73–84
26. Maute K, Frangopol D M. Reliability-based design of MEMS mechanisms by topology optimization. Computers & Structures, 2003, 81(8–11): 813–824
27. Lazarov B S, Schevenels M, Sigmund O. Topology optimization considering material and geometric uncertainties using stochastic collocation methods. Structural and Multidisciplinary Optimization, 2012, 46(4): 597–612
28. Doltsinis I, Kang Z. Robust design of structures using optimization methods. Computer Methods in Applied Mechanics and Engineering, 2004, 193(23–26): 2221–2237
29. Sandgren E, Cameron T M. Robust design optimization of structures through consideration of variation. Computers & Structures, 2002, 80(20–21): 1605–1613
30. Asadpoure A, Tootkaboni M, Guest J K. Robust topology optimization of structures with uncertainties in stiffness—Application to truss structures. Computers & Structures, 2011, 89(11–12): 1131–1141
31. Vanmarcke E. Random Fields: Analysis and Synthesis. Singapore: World Scientific Publishing, 2010
32. Jiang C, Li W, Han X, et al. Structural reliability analysis based on random distributions with interval parameters. Computers & Structures, 2011, 89(23–24): 2292–2302
33. Do D M, Gao W, Song C, et al. Interval spectral stochastic finite element analysis of structures with aggregation of random field and bounded parameters. International Journal for Numerical Methods in Engineering, 2016, 108(10): 1198–1229
34. Ying X, Lee S, Chen W, et al. Efficient random field uncertainty propagation in design using multiscale analysis. Journal of Mechanical Design, 2009, 131(2): 021006
35. Luo Y, Zhan J, Xing J, et al. Non-probabilistic uncertainty quantification and response analysis of structures with a bounded field model. Computer Methods in Applied Mechanics and Engineering, 2019 (in press)
36. Svanberg K. The method of moving asymptotes—A new method for structural optimization. International Journal for Numerical Methods in Engineering, 1987, 24(2): 359–373
37. Sigmund O. Morphology-based black and white filters for topology optimization. Structural and Multidisciplinary Optimization, 2007, 33(4–5): 401–424
38. Wang F, Lazarov B S, Sigmund O. On projection methods, convergence and robust formulations in topology optimization. Structural and Multidisciplinary Optimization, 2011, 43: 767–784